Title

Enhanced yield-mobility products in hybrid halide Ruddlesdenâ��Popper compounds with aromatic ammonium spacers

Journal

Dalton Transactions, 48(37)

ISSN

1477-9226 1477-9234

Authors

Venkatesan, Naveen R
Mahdi, Ali
Barraza, Brian
et al.

Publication Date

2019

DOI

10.1039/C9DT03074C

Peer reviewed

Enhanced Yield-Mobility Products in Hybrid Halide Ruddlesden–Popper Compounds with Aromatic Ammonium Spacers†

Naveen R. Venkatesan,[a] Ali Mahdi,[bc] Brian Barraza,[c] Guang Wu,[c]

Michael L. Chabinyc,[*ab] and Ram Seshadri[*abc]

[a] Materials Department, University of California, Santa Barbara, California 93106, United States

[b] Materials Research Laboratory, University of California, Santa Barbara, California 93106, United States

[c] Department of Chemistry and Biochemistry, University of California, Santa Barbara, California 93106, United States

†Electronic supplementary information (ESI) available: Single-crystal diffraction images, bond lengths and angles in crystal structures, comparison of powder XRD patterns to isotropic and textured simulations, and comparison of diffraction to PbI_2 showing no degradation and crystal structures of $(BPEA)_2PbI_4$ and $(BPEA)_2(MA)Pb_2I_7$ solved at 100 K

ABSTRACT

Hybrid halide Ruddlesden–Popper compounds are related to three-dimensional hybrid AMX_3 perovskites (e.g. where A is a monovalent cation, M is a divalent metal cation, and X is a halogen) with the general formula $L_2A_{n-1}M_nX_{3n+1}$ where L is a monovalent spacer cation. The crystal structure comprises perovskite-like layers separated by organic cation spacers. Here two Ruddlesden–Popper compounds with a conjugated cation, 2-(4-biphenyl)ethylammonium (BPEA) prepared by solvothermal and solvent evaporation techniques are reported. The structures of the two compounds: $(BPEA)_2PbI_4$ and $(BPEA)_2(CH_3NH_3)Pb_2I_7$, were solved by X-ray crystallography. The aromatic rings of the BPEA groups are well-separated in the organic layers leading to optical properties comparable to n = 1 and 2 hybrid halide Ruddlesden–Popper compounds with simpler alkyl ammonium cations. The ambient stability of both compounds over time was also confirmed by powder X-ray diffraction. Finally, the transient photoconductance, measured by time-resolved microwave conductivity, show that the compounds have maximum yield-mobility products respectively of 0.07 $cm^2\ V^{-1}\ s^{-1}$ and 1.11 $cm^2\ V^{-1}\ s^{-1}$ for $(BPEA)_2PbI_4$ and $(BPEA)_2(CH_3NH_3)Pb_2I_7$, both slightly enhanced over what has been measured for compounds with simpler (*n*-butylammonium) spacer cations.

INTRODUCTION

Hybrid organic-inorganic perovskites (HOIPs) are solution-processable semiconductors with a diversity of structures allowed by the combination of organic and inorganic groups.[1–7] The power conversion efficiency (PCE) of photovoltaic devices composed of hybrid perovskite alloys (based on $CH_3NH_3PbI_3$ and $FAPbI_3$) has increased to 23.7% very quickly,[8] competitive with other thin film technologies such as CIGS and CdTe.[9,10] Additionally, HOIPs have shown great synthetic tunability, allowing control of emission energies, making them promising for light emission applications.[11–20] However, three-dimensional hybrid perovskites have been shown to be susceptible to degradation from heat, light, and moisture, hampering their long-term device stability.[21–26]

The class of two-dimensional layered perovskite compounds known as Ruddlesden–Popper (R–P) compounds, have been synthesized using organic ammonium and main group cations and halide anions. These compounds usually display enhanced stability in ambient conditions.[27–30] The R–P compounds have a general stochiometric formula of $(L)_2(CH_3NH_3)_{n-1}Pb_nI_{3n+1}$, where L represents a large organic cation that serves to break up the three-dimensional connectivity of the perovskite crystal structure and n represents the number of lead iodide octahedra in the inorganic layer.[31,32] The enhanced stability of R–P perovskites has been attributed to the increased hydrophobicity from the organic layer from by the L cations.[33–35] The addition of this organic layer, however, leads to highly anisotropic charge transport, and devices based on two-dimensional perovskites have only achieved PCE values close to 15%.[28,36] Purely two-dimensional perovskites have wider band gaps than three-dimensional perovskites providing a means to tune emission in light emitting diodes.[14,15,17] Recent efforts to embed two-dimensional perovskite moieties into the overall three-dimensional perovskite matrix have also yielded efficiencies closer to that of champion devices, with some increased stability.[37–39] The majority of studies have focused on alkylammonium L

cations, and these compounds have resulted in the highest photovoltaic efficiencies to date for two-dimensional perovskite compounds.[28,33,40–42] Various conjugated ions have also been incorporated into the Ruddlesden–Popper structure,[12,43,44] including thiophenes,[45,46] and the single phenyl analog of the structures reported here, phenethylammonium.[27,47] Finally, recent efforts have embraced other layered perovskite motifs such as Dion–Jacobson compounds.[48,49] Controlling the properties of lower dimensional perovskites by varying the *L* cation is desirable for tuning the electronic properties of the materials system either in pure systems or in composites.

We report here two Ruddlesden–Popper compounds using the aromatic organic cation 2-(4-biphenyl)ethylammonium (BPEA), resulting in the compounds $(BPEA)_2PbI_4$ (n = 1) and $(BPEA)_2(CH_3NH_3)Pb_2I_7$ (n = 2). These compounds were synthesized by solvothermal and solvent evaporation techniques, and the resulting crystal structures were solved from X-ray crystallography. Structural measurements after aging in ambient conditions show that both compounds are stable without encapsulation. The optical absorbance was measured with ultraviolet-visible spectroscopy, and the charge transport was characterized by time-resolved microwave conductivity (TRMC). By utilizing TRMC, carrier dynamics in the synthesized powders could directly be measured without device formation.

EXPERIMENTAL SECTION

$(BPEA)_2PbI_4$ preparation. Single crystals of $(BPEA)_2PbI_4$ were prepared through solvothermal methods. A stoichiometric ratio of lead (II) iodide (PbI_2, 100 mg), 2-(4-biphenyl)ethylamine (BPEA, 85.6 mg), and aqueous (57 wt% in H_2O) hydroiodic acid (HI, 1 mL) were added to a pressure vessel (23 mL PTFE-lined stainless steel Parr autoclave). The temperature of the reaction vessel was ramped to 150°C over 2 hours, held for 8 hours, and then allowed to cool to room

temperature over 2 hours. Resulting crystals were then washed with diethyl ether ($(C_2H_5)_2O$) and dried under vacuum for one day.

$(BPEA)_2(CH_3NH_3)Pb_2I_7$ preparation. Single crystals of $(BPEA)_2(CH_3NH_3)Pb_2I_7$ were prepared *via* solvent evaporation – a stoichiometric ratio of previously synthesized $(BPEA)_2PbI_4$ (30 mg), PbI_2 (24.9 mg), and methylammonium iodide (CH_3NH_3I, 8.6 mg) were dissolved in a 2:1 mixture (volume/volume) of acetone and nitromethane (15 mL). The mixture was stirred and heated at 90°C to form a pale-yellow solution. The solvent was allowed to evaporate at room temperature over six days, yielding bright, red crystals.

Single-Crystal X-Ray Diffraction. Single-crystal X-ray diffraction (SC-XRD) data was collected for each of the two Ruddlesden–Popper compounds with a Bruker KAPPA APEX II diffractometer equipped with an APEX II CCD detector utilizing a TRIUMPH monochromator and a Mo-Kα X-ray source (λ = 0.71073 Å). The crystals were mounted on a cryoloop with Paratone-N oil. The multi-scan method, SADABS, was used for absorption correction of the data.[50] Further calculations were done using SHELXTL.[51] The low bond precision in carbon bonds is due to the disorder and poor contrast near to heavier elements. Structures were determined using direct methods,[52] and the graphical depictions of crystal structures shown were created with VESTA.[53]

Powder X-Ray Diffraction. Powder X-ray diffraction (PXRD) was measured using a Panalytical Empyrean powder diffractometer in reflection mode with a Cu- Kα source, operating with an accelerating voltage of 45 kV and a beam current of 40 mA. Simulated diffraction patterns were calculated using the General Structure Analysis System (GSAS).[54] For simulated diffraction

patterns containing preferred orientation, March–Dollase orientational correction factors were used.[55]

Ultraviolet-Visible Spectroscopy. Absorption spectra were determined by grinding crystals into powders and measuring diffuse reflectance with a Shimadzu UV-2600 ultraviolet-visible spectrophotometer equipped with an integrating sphere. Reflectance data were converted to absorbance using the Kubelka-Munk equations.[56]

Time-Resolved Microwave Conductivity. TRMC measurements were conducted with an experimental setup described previously.[57–59] A Sivers IMA VO4280X/00 voltage-controlled oscillator (VCO) (approximate power of 16 dBm and a tunable frequency range of 8–15 GHz) was used to generate a microwave frequency signal. The signal was then directed into a Fairview Microwave SFC0712 electronic circulator, a three-port device that rotates signals from port 1 to port 2 and signals from port 2 to port 3. The signal from port 2 was then fed into a Fairview Microwave 90AC206 SMA to X-band waveguide and is coupled to an X-band cavity with homebuilt coupling iris and tuning screw. The cavity operates in TE_{103} mode, and a homemade copper plate with slots along direction of microwave current allows optical access to the sample. The microwaves form standing waves and the tuning screw allows for over coupling, critical coupling, and under coupling to the cavity – all experiments reported were performed in the under coupled regime. The powder samples were mounted to the inside of the cavity with double-sided tape and placed at the maximum of the microwave electric field. Reflected microwaves are directed to a Fairview Microwave SMD0218 zero-bias Schottky diode detector, operating in the linear regime. The rectified signal was amplified by a three stage, DC-coupled wide-band amplifier

consisting of Texas Instruments THS3091 operational amplifiers. For the reference signal, the microwave signal was split at the source to normalize the reflected power from the cavity. The amplified signal and reference were detected using a Textronix TDS 3032C digital oscilloscope. Free carriers are generated in the powder samples through illumination with a Continuum Minilite pulsed Nd:YAG 532 nm laser (FWHM of ~5 ns), which drift under the influence of the microwave signal with a velocity proportional to their mobility ($v = \mu E$). The change in reflected microwave intensity is then used to determine the transient photoconductance which, in turn, is used to calculate the TRMC figure-of-merit: $\phi\Sigma\mu$ (yield-mobility product) at each fluence.[60]

RESULTS AND DISCUSSION

The structures of $(BPEA)_2PbI_4$ and $(BPEA)_2(CH_3NH_3)Pb_2I_7$, solved from single-crystal X-ray diffraction at 100 K, are shown in Figure 1, visualized along the [010] crystallographic direction for $(BPEA)_2PbI_4$ and [001] for $(BPEA)_2(CH_3NH_3)Pb_2I_7$ using VESTA.[53] Solvothermal synthesis of $(BPEA)_2PbI_4$ was required to produce single-crystals of sufficient size for X-ray crystallography. The parameters of the structure solutions of each compound are shown in Table 1, and single-crystal diffraction images are presented in Section S1 (ESI†). Both compounds have orthorhombic unit cells and the diffraction data were fit best by non-centrosymmetric space groups. The organic BPEA moieties form symmetric bilayers in both compounds, while the inorganic framework in the two perovskites consists of corner-sharing lead iodide octahedra. The organic bilayer formed between the lead iodide sheets is consistent with previously reported hybrid halide Ruddlesden–Popper structures with other organic cation spacers.[28,45,47,61,62] The BPEA moieties from subsequent layers do not interdigitate, preventing π-π interactions between *L* groups on each lead iodide layer. If we consider that the *n*-butylammonium cation would fit into a cylinder with a diameter of ~1.5 Å and it forms a bilayer structure rather than interdigitating, it is

unsurprising that 2-(4-biphenyl)ethylammonium which packs with a closest C-C distance between phenyl rings of ~3.4 Å, also forms separate layers. The widest region of the phenyl ring has a diameter of ~4 Å, so this aromatic packing distance is required when accounting for bond rotations. The separation distance between the lead iodide layers is ~15 Å in $(BPEA)_2PbI_4$ and $(BPEA)_2(CH_3NH_3)Pb_2I_7$, compared to ~10 Å in $(PEA)_2PbI_4$ and $(PEA)_2(CH_3NH_3)Pb_2I_7$.[44,62] There is a slight difference in the layer spacing between the BPEA $n = 1$ (15.0 Å) and $n = 2$ (14.7 Å) that may be due to slightly more efficient packing in the $n = 2$ compound; regardless, the organic layers appear to be consistent in size. Geometric details of both crystal structures, including bond lengths and angles are tabulated in Table S1 (ESI†). The octahedra in the lead iodide layers in both $(BPEA)_2PbI_4$ and $(BPEA)_2(CH_3NH_3)Pb_2I_7$ are highly tilted in plane, with equatorial Pb-I-Pb bond angles of approximately 155° in both structures. The measured bond lengths in both compounds are consistent (i.e. independent of *L* cation used) with previous observations in other hybrid halide Ruddlesden–Popper compounds, however the out of plane tilt between connected Pb-I octahedra (in the $n = 2$) are much stiffer (179.2°) compared to $(BA)_2(CH_3NH_3)Pb_2I_7$ (165.6°).[45,63]

Table 1. Crystallographic Data for $(BPEA)_2PbI_4$ and $(BPEA)_2(CH_3NH_3)Pb_2I_7$ at 100 K.

Empirical Formula	$(BPEA)_2PbI_4$	$(BPEA)_2(CH_3NH_3)Pb_2I_7$
Crystal Habit and Color	plate, orange	plate, red
Crystal System	orthorhombic	orthorhombic
Space Group (#)	*Cmc2₁* (36)	*Aba2* (41)
Volume (Å^3)	3250.8(8)	4199.5(6)
Temperature (K)	100(2)	100(2)
a (Å)	42.920(6)	8.7633(8)
b (Å)	8.7431(11)	55.030(5)
c (Å)	8.6629(14)	8.7081(7)
α (°)	90	90
β (°)	90	90
γ (°)	90	90
Z	4	4
ρ (g mol^{-1})	1107.32	1731.30
Dens. (g cm^{-3})	2.263	2.738
Abs. (mm^{-1})	9.007	13.176
F_{000}	2016	3072
Reflections	10433 (2500)	9269 (3551)
R_{int}	0.0927	0.0861
R_1	0.0533	0.0653
wR_2	0.0892	0.1471
∂F (e Å^{-3})	2.612 & -1.446	4.473 & -5.449
GOF	1.436	1.095

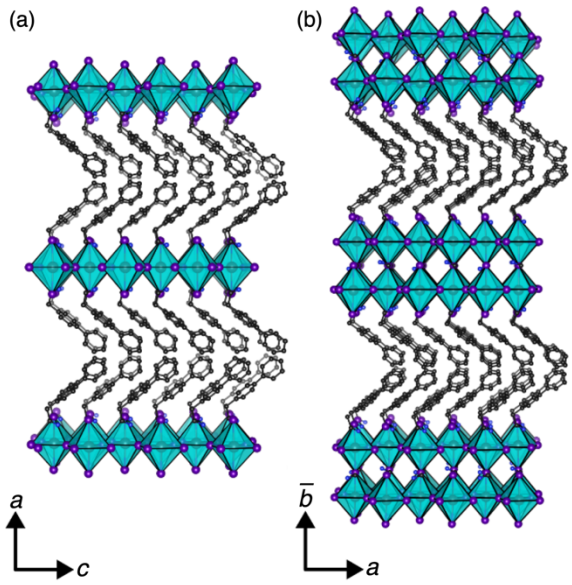

Figure 1. (a) Crystal structures of $(BPEA)_2PbI_4$ and (b) $(BPEA)_2(CH_3NH_3)Pb_2I_7$ solved by single-crystal X-ray diffraction, projected down the *b* and *c* crystallographic axes, respectively. The BPEA cations pack diagonally, are eclipsed with each other, and do not interdigitate.

Because bulk characterization measurements were carried on powders consisting of crushed single-crystals, solved crystal structures were used to simulate powder X-ray diffraction (PXRD) patterns for comparison. Simulated diffraction patterns were generated as described in the Experimental Section. Figure 2 shows PXRD measurements of crushed crystals of $(BPEA)_2PbI_4$ and $(BPEA)_2(CH_3NH_3)Pb_2I_7$ both immediately after preparation and after five weeks of aging in ambient conditions, along with their simulated diffraction patterns. To capture the correct structural behavior in $(BPEA)_2(CH_3NH_3)Pb_2I_7$, the simulated diffraction pattern included texturing along the [010] crystallographic direction, which is the lead iodide layer stacking direction (Figure 1). It is possible that due to the tendency of these $n = 2$ crystals to grow as anisotropic flakes, the resulting powder retains some crystalline texture. If the slow growth direction during preparation

was along this stacking direction (due to the incorporation of the BPEA layer), it is consistent with the flake-like crystals. This is evident when compared to a simulation of an isotropic sample of $(BPEA)_2(CH_3NH_3)Pb_2I_7$, in which the relative peak height intensities do not match well with our measurement (Figure S3, ESI†). In both the $n = 1$ and $n = 2$ compounds, the position and intensities of peaks in the diffraction patterns show no change after five weeks of aging. This suggests that $(BPEA)_2(CH_3NH_3)_{n-1}Pb_nI_{3n+1}$ possesses increased stability relative to three-dimensionally connected perovskites, a property that has been widely observed in layered perovskite compounds.[27,28,64] The subtle differences in relative peak heights between the as-synthesized and aged samples is likely due to the slight variations in the overall crystalline texturing from the loading of the powder samples for measurement. Ultimately, the structural measurements on both compounds show no formation of PbI_2 (Figure S4, ESI†) and no other degradation upon aging in ambient conditions.

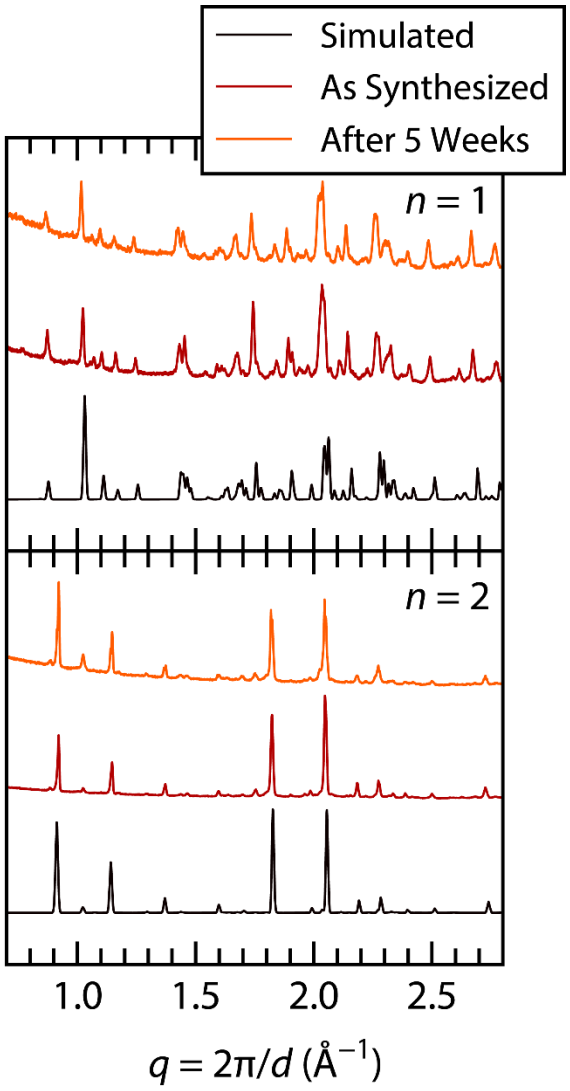

Figure 2. Powder X-ray diffraction (PXRD) patterns of $(BPEA)_2PbI_4$ (n = 1) and $(BPEA)_2(CH_3NH_3)Pb_2I_7$ (n = 2) both after preparation and after five weeks of aging in ambient conditions, along with simulated PXRD patterns of solved structures shown in Figure 1.

The optical absorbances of both layered perovskite compounds were measured and are presented in Figure 3, showing expected behavior. Due to the large optical density of both powder samples, absorbances were measured by taking diffuse reflectance data and transforming them according to the Kubelka-Munk equations.[56] In both cases, clear excitonic features are visible at the optical

absorbance onset, consistent with the quantum confined structure of the Ruddlesden–Popper compounds. In $(BPEA)_2PbI_4$, the peak attributed to excitonic absorption occurs at 2.4 eV, while in $(BPEA)_2(CH_3NH_3)Pb_2I_7$, it appears at 2.2 eV. Both of these energies are equal to previously measured exciton energies in Ruddlesden–Popper systems containing both butylammonium and phenethylammonium spacer groups.[47,57]

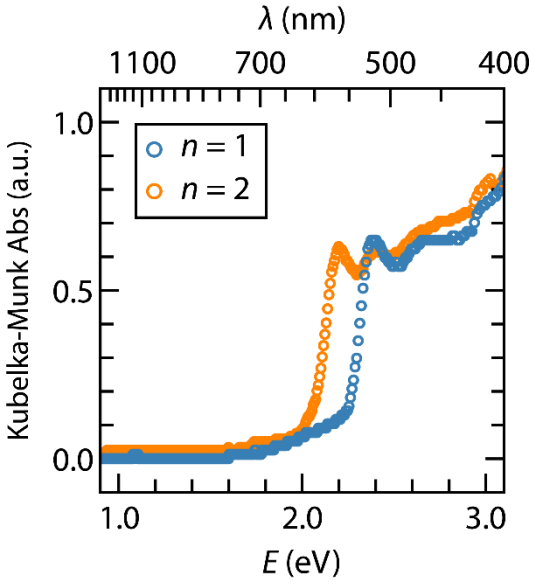

Figure 3. Optical absorbance of $(BPEA)_2PbI_4$ (n = 1) and $(BPEA)_2(CH_3NH_3)Pb_2I_7$ (n = 2) measured from diffuse reflectance of powder samples. Reflectance data were converted into absorbance values using the Kubelka-Munk equations and show excitonic features at 2.4 eV and 2.2 eV for n = 1 and 2, respectively.

The charge carrier dynamics of these two compounds were analyzed using time-resolved microwave conductivity (TRMC).[57,58,65–71] Excitation of the compounds with a pulse of light with energy above the band gap creates free carriers and excitons. Only the free carriers then interact

with the microwave electric field (frequency range of 8 – 9 GHz) and the attenuation of this applied microwave signal, caused by carrier drift, can be then used to calculate the transient photoconductance in the sample. Using these photoconductance measurements, a value of $\phi\Sigma\mu$ can be determined, which is the figure-of-merit for TRMC – $\phi\Sigma\mu$ is the product of ϕ (the yield of free carriers per incident photon) and the sum of the electron and hole mobilities, $\Sigma\mu = \mu_e + \mu_h$. The value of $\phi\Sigma\mu$ at short times after the excitation pulse typically exhibit strong laser fluence dependence due to recombination of electron hole pairs.[65,72] Fluence-dependent measurements of $\phi\Sigma\mu$ were therefore collected for both $(BPEA)_2PbI_4$ and $(BPEA)_2(CH_3NH_3)Pb_2I_7$ and are shown in Figure 4, along with previously measured values for $(BA)_2PbI_4$ and $(BA)_2(CH_3NH_3)Pb_2I_7$.[57] The lowest measurable fluence for both compounds was set by the signal-to-noise of our instrument. Additionally, due the small size of the $(BPEA)_2PbI_4$ and $(BPEA)_2(CH_3NH_3)Pb_2I_7$ crystals, powders were measured rather than single-crystals in order to improve the signal-to-noise of the experiment. The peak yield-mobility products for the n = 1 and 2 compounds are 0.07 $cm^2\ V^{-1}\ s^{-1}$ (at 2.25×10^{13} photons cm^{-2}) and 1.11 $cm^2\ V^{-1}\ s^{-1}$ (at 5.93×10^{12} photons cm^{-2}), respectively.

To understand the TRMC data, we must consider the different charge recombination pathways in both compounds. Charge recombination in semiconductors is governed by the rate equation $R = k_1 n(t) + k_2 n(t)^2 + k_3 n(t)^3$, where $n(t)$ is the instantaneous carrier concentration and k_1, k_2, and k_3 are the rate constants of monomolecular, bimolecular, and trimolecular or Auger recombination, respectively. By changing the incident laser fluence, we can change the carrier concentration and observe the effects of recombination. Therefore, at low carrier concentrations, it is expected that the recombination dynamics are dominated by monomolecular recombination – since this is linear with $n(t)$ in this regime, we would expect the TRMC plot to have a very shallow slope on a logarithmic scale. This behavior is evident in TRMC data of methylammonium lead

iodide at low laser fluences.[57,58,65] As the laser fluence and carrier concentration increases, both bimolecular and Auger recombination pathways become more active and the dependence of $\phi\Sigma\mu$ becomes increasingly more negative. We see an overall monotonic increase in $\phi\Sigma\mu$ with decreasing laser fluence and therefore cannot decouple the monomolecular recombination regime from higher order pathways. This dependence has been observed in previous TRMC measurements of layered hybrid halides and has been attributed to larger higher order recombination rate coefficients.[57,58]

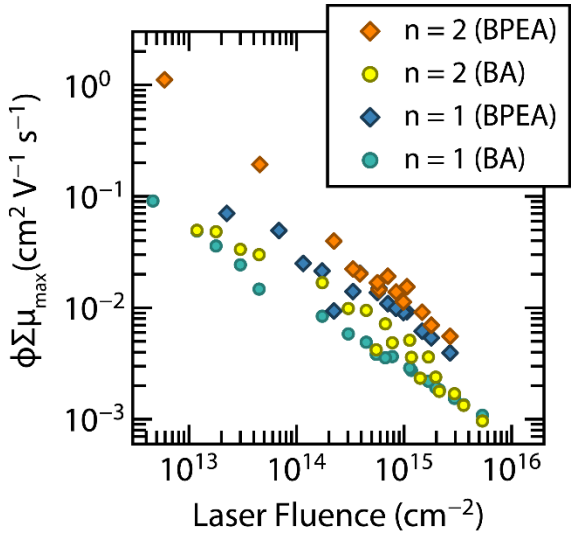

Figure 4. Maximum value of the TRMC figure-of-merit $\phi\Sigma\mu$ over a wide range of excitation laser fluences for $(BPEA)_2PbI_4$ (n = 1) and $(BPEA)_2(CH_3NH_3)Pb_2I_7$ (n = 2), along with TRMC data of $(BA)_2PbI_4$ and $(BA)_2(CH_3NH_3)Pb_2I_7$ from reference 57. Monotonic increases seen with decreasing fluence are characteristic of shorter carrier lifetimes and larger recombination rate coefficients compared to $MAPbI_3$.

At low fluences, the value of $\phi\Sigma\mu$ for the n = 1 BPEA compound is slightly larger than the analogous *n*-butylammonium (BA) Ruddlesden–Popper compound. For $(BPEA)_2(CH_3NH_3)Pb_2I_7$,

the value of $\phi\Sigma\mu$ is approximately an order of magnitude higher than for $(BA)_2(CH_3NH_3)Pb_2I_7$. From the absorbance data, it appears that changes in dielectric confinement effects from the different *L* ions does not affect the energy of the excitonic absorption onset. However, the difference in the dielectric constant of BPEA compared to an alkylammonium chain could decrease the exciton binding energy, promoting increased free carrier formation. Measurements on $n = 1$ and 2 were done on powders, but the measured mobility values are biased towards the in-plane mobilities (carrier motion within the Pb-I sheets), which are much higher than the out-of-plane (between subsequent Pb-I sheets) mobilities since the electronic coupling between layers in R–P compounds has shown to be weak.[28,63,73,74] In contrast, the TRMC measurements of $(BA)_2PbI_4$ and $(BA)_2(CH_3NH_3)Pb_2I_7$ were performed on thin films. However, these films were found to be highly textured – the phase fractions corresponding to lead iodide layers being oriented in-plane (parallel to substrate surface) were $f = 1.0$ in $n = 1$ and $f = 0.75$ in $n = 2$, respectively.[57] Therefore, the thin film measurements should also yield values that are highly biased towards the in-plane mobilities. In the $(BPEA)_2PbI_4$ compound, the laser excitation consists of photons with energy (2.33 eV) slightly below the excitonic peak energy (2.4 eV) due to limitations in our experimental setup, but there is still measured absorbance, as shown in Figure 3. This results in an extremely small value of ϕ that makes comparison with $(BA)_2PbI_4$ difficult, which also likely has a small value of ϕ due to also having an absorption onset of 2.4 eV. However, we do observe that the TRMC data for the BPEA $n = 1$ compound are consistently higher than that of the corresponding BA (Figure 4). The $n = 2$ $(BPEA)_2(CH_3NH_3)Pb_2I_7$ compound on the other hand, appears to have a much larger value of $\phi\Sigma\mu$ (0.19 $cm^2\ V^{-1}\ s^{-1}$ at 4.56×10^{13} photons cm^{-2}), than the corresponding $(BA)_2(CH_3NH_3)Pb_2I_7$ at a comparable fluence (0.03 $cm^2\ V^{-1}\ s^{-1}$ at 4.49×10^{13} photons cm^{-2}). In both cases, it is difficult to make a direct comparison without knowing the value of ϕ, but we can

speculate on the origin of the increased TRMC signal. Since 75% of the domains in the $(BA)_2(CH_3NH_3)Pb_2I_7$ film are oriented to measure in-plane transport, even if all of the $(BPEA)_2(CH_3NH_3)Pb_2I_7$ powder was textured with the lead iodide domains oriented parallel to the microwave electric field, it would not solely account for the large difference between the two $\phi\Sigma\mu$ values, assuming similar carrier yields and mobilities. This suggests that the BPEA R–P compounds may either have a larger carrier mobility or carrier yield than the BA systems, when measured by the same TRMC technique. Yield-mobility products measured from TRMC can be affected by the grain size, which is ~μm scale for the BPEA powders and was ~100 nm in the BA films, however, this effect has been shown to be minimal above 100 nm in $CH_3NH_3PbI_3$.[75] The increased TRMC signal in both BPEA compounds can also be attributed to a lowering of the exciton binding energy due to the increase in the dielectric constant. This difference in effective dielectric could also have an effect on carrier mobility within the lead iodide sheets, accounting for some of the increase. An alternative explanation is that the slower solvothermal crystal growth results in BPEA crystals with a lower defect concentration than the highly non-equilibrium spin-coating of the BA thin films, but they both show a monotonic increase in $\phi\Sigma\mu$ with decreasing laser fluence, which is suggestive of short carrier lifetimes and large recombination rate constants.[57] Although it is unclear whether functionalization of the organic layer is the reason for this increased yield-mobility product, it would appear that the use of the aromatic ammonium cations improves carrier transport relative to that of a straight alkyl chain. Our result suggests that using a higher dielectric constant organic as a spacer molecule in Ruddlesden–Popper compounds can improve the overall transport properties.

CONCLUSIONS

Two hybrid Ruddlesden–Popper compounds with a 2-(4-biphenyl)ethylammonium cationic spacer were prepared using solvothermal and solvent evaporation techniques. The two structures, $(BPEA)_2PbI_4$ and $(BPEA)_2(CH_3NH_3)Pb_2I_7$, were solved by X-ray crystallography and correspond to the n = 1 and 2 compounds of the general formula $(BPEA)_2(MA)_{n-1}Pb_nI_{3n+1}$. Both compounds form in the expected Ruddlesden–Popper structures with a bilayer of the larger organic cations separating the lead iodide inorganic layers. Structural measurements from X-ray diffraction on the as-synthesized and aged powders showed material stability in ambient conditions. Optical properties of both compounds were measuring by diffuse reflectance and show highly excitonic absorption and optical bandgaps consistent with other n = 1 and n = 2 layered R–P compounds. Finally, time-resolved microwave conductivity was used to measure the charge transport properties. The contactless TRMC technique allowed us to directly measure carrier dynamics of the perovskite powders without the need to cast films or prepare devices. The yield-mobility products measured by TRMC were compared to those from the $(BA)_2(CH_3NH_3)_{n-1}Pb_nI_{3n+1}$ R–P series and were found to possess comparable values in the n = 1 compounds but are an order of magnitude higher in n = 2. It is unclear whether this increase is directly due to the presence of the aromatic groups in the organic spacer cations, but it appears that the use of a higher dielectric constant organic spacer can improve the transport properties of Ruddlesden–Popper perovskite materials.

CONFLICTS OF INTEREST

There are no conflicts to declare.

ACKNOWLEDGMENT

The authors thank Emily Levin for assistance with initial stages of the manuscript, and Dr. Clayton Dahlman, Rhys Kennard, and Ryan DeCrescent for insightful discussions. This work was supported by the U.S. Department of Energy, Office of Science, Basic Energy Sciences under award number DE-SC-0012541. Development of the microwave conductivity instrument was supported by the Defense Threat Reduction Agency under Award Number HDTRA1-15-0023. The research reported here made use of the shared facilities of the Materials Research Science and Engineering Center (MRSEC) at UC Santa Barbara through NSF DMR 1720256. The UC Santa Barbara MRSEC is a member of the Materials Research Facilities Network (www.mrfn.org).

REFERENCES

1 G. C. Papavassiliou, G. A. Mousdis and I. B. Koutselas, *Adv. Mater. Opt. Electron.*, 1999, **9**, 265–271.

2 B. Saparov and D. B. Mitzi, *Chem. Rev.*, 2016, **116**, 4558–4596.

3 J. Berry, T. Buonassisi, D. A. Egger, G. Hodes, L. Kronik, Y.-L. Loo, I. Lubomirsky, S. R. Marder, Y. Mastai, J. S. Miller, D. B. Mitzi, Y. Paz, A. M. Rappe, I. Riess, B. Rybtchinski, O. Stafsudd, V. Stevanovic, M. F. Toney, D. Zitoun, A. Kahn, D. Ginley and D. Cahen, *Advanced Materials*, 2015, **27**, 5102–5112.

4 W. Zhang, G. E. Eperon and H. J. Snaith, *Nature Energy*, 2016, **1**, 16048.

5 D. B. Mitzi, K. Chondroudis and C. R. Kagan, *IBM Journal of Research and Development*, 2001, **45**, 29–45.

6 D. B. Mitzi, L. L. Kosbar, C. E. Murray, M. Copel and A. Afzali, *Nature*, 2004, **428**, 299–303.

7 D. B. Mitzi, C. A. Feild, W. T. A. Harrison and A. M. Guloy, *Nature*, 1994, **369**, 467–469.

8 W. S. Yang, B.-W. Park, E. H. Jung, N. J. Jeon, Y. C. Kim, D. U. Lee, S. S. Shin, J. Seo, E. K. Kim, J. H. Noh and S. I. Seok, *Science*, 2017, **356**, 1376–1379.

9 A. Polman, M. Knight, E. C. Garnett, B. Ehrler and W. C. Sinke, *Science*, 2016, **352**, aad4424.

10 M. A. Green, K. Emery, Y. Hishikawa, W. Warta, E. D. Dunlop, D. H. Levi and A. W. Y. Ho-Baillie, *Prog. Photovolt: Res. Appl.*, 2017, **25**, 3–13.

11 M. Yuan, L. N. Quan, R. Comin, G. Walters, R. Sabatini, O. Voznyy, S. Hoogland, Y. Zhao, E. M. Beauregard, P. Kanjanaboos, Z. Lu, D. H. Kim and E. H. Sargent, *Nature Nanotechnology*, 2016, **11**, 872–877.

12 N. Wang, L. Cheng, R. Ge, S. Zhang, Y. Miao, W. Zou, C. Yi, Y. Sun, Y. Cao and R. Yang, *Nature Photonics*, 2016, **10**, 699.

13 K. Lin, J. Xing, L. N. Quan, F. P. G. de Arquer, X. Gong, J. Lu, L. Xie, W. Zhao, D. Zhang and C. Yan, *Nature*, 2018, **562**, 245.

14 Z. Xiao, R. A. Kerner, L. Zhao, N. L. Tran, K. M. Lee, T.-W. Koh, G. D. Scholes and B. P. Rand, *Nature Photonics*, 2017, **11**, 108–115.

15 M. V. Kovalenko, L. Protesescu and M. I. Bodnarchuk, *Science*, 2017, **358**, 745–750.

16 L. Protesescu, S. Yakunin, M. I. Bodnarchuk, F. Krieg, R. Caputo, C. H. Hendon, R. X. Yang, A. Walsh and M. V. Kovalenko, *Nano letters*, 2015, **15**, 3692–3696.

17 M. C. Weidman, A. J. Goodman and W. A. Tisdale, *Chemistry of Materials*, 2017, **29**, 5019–5030.

18 M. D. Smith and H. I. Karunadasa, *Acc. Chem. Res.*, 2018, **51**, 619–627.

19 M. D. Smith, A. Jaffe, E. R. Dohner, A. M. Lindenberg and H. I. Karunadasa, *Chem. Sci.*, 2017, **8**, 4497–4504.

20 R. M. Kennard, C. J. Dahlman, H. Nakayama, R. A. DeCrescent, J. A. Schuller, R. Seshadri, K. Mukherjee and M. L. Chabinyc, *ACS Applied Materials & Interfaces*, 2019, **11**, 25313–25321.

21 G. Divitini, S. Cacovich, F. Matteocci, L. Cinà, A. Di Carlo and C. Ducati, *Nature Energy*, 2016, **1**, 15012.

22 E. Mosconi, J. M. Azpiroz and F. De Angelis, *Chem. Mater.*, 2015, **27**, 4885–4892.

23 Y. Li, X. Xu, C. Wang, B. Ecker, J. Yang, J. Huang and Y. Gao, *J. Phys. Chem. C*, 2017, **121**, 3904–3910.

24 N. Aristidou, I. Sanchez-Molina, T. Chotchuangchutchaval, M. Brown, L. Martinez, T. Rath and S. A. Haque, *Angew. Chem. Int. Ed.*, 2015, **54**, 8208–8212.

25 T. Abraha Berhe, W.-N. Su, C.-H. Chen, C.-J. Pan, J.-H. Cheng, H.-M. Chen, M.-C. Tsai, L.-Y. Chen, A. Aregahegn Dubale and B.-J. Hwang, *Energy & Environmental Science*, 2016, **9**, 323–356.

26 X. Zhao and N.-G. Park, *Photonics*, 2015, **2**, 1139–1151.

27 I. C. Smith, E. T. Hoke, D. Solis-Ibarra, M. D. McGehee and H. I. Karunadasa, *Angewandte Chemie*, 2014, **126**, 11414–11417.

28 H. Tsai, W. Nie, J.-C. Blancon, C. C. Stoumpos, R. Asadpour, B. Harutyunyan, A. J. Neukirch, R. Verduzco, J. J. Crochet, S. Tretiak, L. Pedesseau, J. Even, M. A. Alam, G. Gupta, J. Lou, P. M. Ajayan, M. J. Bedzyk, M. G. Kanatzidis and A. D. Mohite, *Nature*, 2016, **536**, 312–316.

29 L. Pedesseau, D. Sapori, B. Traore, R. Robles, H.-H. Fang, M. A. Loi, H. Tsai, W. Nie, J.-C. Blancon, A. Neukirch, S. Tretiak, A. D. Mohite, C. Katan, J. Even and M. Kepenekian, *ACS Nano*, 2016, **10**, 9776–9786.

30 X. Zhang, G. Wu, S. Yang, W. Fu, Z. Zhang, C. Chen, W. Liu, J. Yan, W. Yang and H. Chen, *Small*, 2017, **13**, 1700611.

31 S. N. Ruddlesden and P. Popper, *Acta Cryst, Acta Crystallogr*, 1957, **10**, 538–539.

32 S. N. Ruddlesden and P. Popper, *Acta Cryst, Acta Crystallogr*, 1958, **11**, 54–55.

33 Y. Chen, Y. Sun, J. Peng, J. Tang, K. Zheng and Z. Liang, *Advanced Materials*, 2017, **30**, 1703487.

34 Y. Chen, S. Yu, Y. Sun and Z. Liang, *The Journal of Physical Chemistry Letters*, 2018, **9**, 2627–2631.

35 T. M. Koh, B. Febriansyah and N. Mathews, *Chem*, 2017, **2**, 326–327.

36 Y. Chen, Y. Sun, J. Peng, W. Zhang, X. Su, K. Zheng, T. Pullerits and Z. Liang, *Adv. Energy Mater.*, 2017, **7**, 1700162.

37 Y. Liu, S. Akin, L. Pan, R. Uchida, N. Arora, J. V. Milić, A. Hinderhofer, F. Schreiber, A. R. Uhl, S. M. Zakeeruddin, A. Hagfeldt, M. I. Dar and M. Grätzel, *Science Advances*, 2019, **5**, eaaw2543.

38 Z. Wang, Q. Lin, F. P. Chmiel, N. Sakai, L. M. Herz and H. J. Snaith, *Nature Energy*, 2017, **6**, nenergy2017135.

39 J.-W. Lee, Z. Dai, T.-H. Han, C. Choi, S.-Y. Chang, S.-J. Lee, N. D. Marco, H. Zhao, P. Sun, Y. Huang and Y. Yang, *Nature Communications*, 2018, **9**, 3021.

40 R. Hamaguchi, M. Yoshizawa-Fujita, T. Miyasaka, H. Kunugita, K. Ema, Y. Takeoka and M. Rikukawa, *Chem. Commun.*, 2017, **53**, 4366–4369.

41 D. Yu, F. Cao, Y. Shen, X. Liu, Y. Zhu and H. Zeng, *The Journal of Physical Chemistry Letters*, 2017, **8**, 2565–2572.

42 M. C. Weidman, M. Seitz, S. D. Stranks and W. A. Tisdale, *ACS Nano*, 2016, **10**, 7830–7839.

43 Z. Chen, C. Zhang, X.-F. Jiang, M. Liu, R. Xia, T. Shi, D. Chen, Q. Xue, Y.-J. Zhao, S. Su, H.-L. Yip and Y. Cao, *Advanced Materials*, 2017, **29**, 1603157.

44 K. Du, Q. Tu, X. Zhang, Q. Han, J. Liu, S. Zauscher and D. B. Mitzi, *Inorg. Chem.*, 2017, **56**, 9291–9302.

45 D. B. Mitzi, *Journal of the Chemical Society, Dalton Transactions*, 2001, **0**, 1–12.

46 D. B. Mitzi, K. Chondroudis and C. R. Kagan, *Inorg. Chem.*, 1999, **38**, 6246–6256.

47 R. L. Milot, R. J. Sutton, G. E. Eperon, A. A. Haghighirad, J. Martinez Hardigree, L. Miranda, H. J. Snaith, M. B. Johnston and L. M. Herz, *Nano Letters*, 2016, **16**, 7001–7007.

48 L. Mao, W. Ke, L. Pedesseau, Y. Wu, C. Katan, J. Even, M. R. Wasielewski, C. C. Stoumpos and M. G. Kanatzidis, *Journal of the American Chemical Society*, 2018, **140**, 3775–3783.

49 Y. Li, J. V. Milić, A. Ummadisingu, J.-Y. Seo, J.-H. Im, H.-S. Kim, Y. Liu, M. I. Dar, S. M. Zakeeruddin and P. Wang, *Nano Letters*, 2018, **19**, 150–157.

50 G. M. Sheldrick, *SADABS*, University of Göttingen, Germany, 1996.

51 G. M. Sheldrick, *Acta Cryst C*, 2015, **71**, 3–8.

52 H. Hauptman, *Current Opinion in Structural Biology*, 1997, **7**, 672–680.

53 K. Momma and F. Izumi, *Journal of Applied Crystallography*, 2011, **44**, 1272–1276.

54 B. H. Toby and R. B. Von Dreele, *J Appl Cryst, J Appl Crystallogr*, 2013, **46**, 544–549.

55 W. A. Dollase, *Journal of Applied Crystallography*, 1986, **19**, 267–272.

56 P. Kubelka and F. Munk, *Z. Tech. Phys*.

57 N. R. Venkatesan, J. G. Labram and M. L. Chabinyc, *ACS Energy Lett.*, 2018, **3**, 380–386.

58 J. G. Labram, N. R. Venkatesan, C. J. Takacs, H. A. Evans, E. E. Perry, F. Wudl and M. L. Chabinyc, *J. Mater. Chem. C*, 2017, **5**, 5930–5938.

59 J. G. Labram and M. L. Chabinyc, *Journal of Applied Physics*, 2017, **122**, 065501.

60 T. J. Savenije, A. J. Ferguson, N. Kopidakis and G. Rumbles, *The Journal of Physical Chemistry C*, 2013, **117**, 24085–24103.

61 N. R. Venkatesan, R. M. Kennard, R. A. DeCrescent, H. Nakayama, C. J. Dahlman, E. E. Perry, J. A. Schuller and M. L. Chabinyc, *Chemistry of Materials*, , DOI:10.1021/acs.chemmater.8b03832.

62 J. Calabrese, N. L. Jones, R. L. Harlow, N. Herron, D. L. Thorn and Y. Wang, *J. Am. Chem. Soc.*, 1991, **113**, 2328–2330.

63 C. C. Stoumpos, D. H. Cao, D. J. Clark, J. Young, J. M. Rondinelli, J. I. Jang, J. T. Hupp and M. G. Kanatzidis, *Chemistry of Materials*, 2016, **28**, 2852–2867.

64 G. Grancini, C. Roldán-Carmona, I. Zimmermann, E. Mosconi, X. Lee, D. Martineau, S. Narbey, F. Oswald, F. D. Angelis, M. Graetzel and M. K. Nazeeruddin, *Nature Communications*, 2017, **8**, ncomms15684.

65 H. Oga, A. Saeki, Y. Ogomi, S. Hayase and S. Seki, *J. Am. Chem. Soc.*, 2014, **136**, 13818–13825.

66 T. J. Savenije, C. S. Ponseca, L. Kunneman, M. Abdellah, K. Zheng, Y. Tian, Q. Zhu, S. E. Canton, I. G. Scheblykin, T. Pullerits, A. Yartsev and V. Sundström, *J. Phys. Chem. Lett.*, 2014, **5**, 2189–2194.

67 E. M. Hutter, M. C. Gélvez-Rueda, A. Osherov, V. Bulović, F. C. Grozema, S. D. Stranks and T. J. Savenije, *Nature Materials*, 2016, **16**, 115–120.

68 C. S. Ponseca, T. J. Savenije, M. Abdellah, K. Zheng, A. Yartsev, T. Pascher, T. Harlang, P. Chabera, T. Pullerits, A. Stepanov, J.-P. Wolf and V. Sundström, *J. Am. Chem. Soc.*, 2014, **136**, 5189–5192.

69 R. Brenes, D. Guo, A. Osherov, N. K. Noel, C. Eames, E. M. Hutter, S. K. Pathak, F. Niroui, R. H. Friend and M. S. Islam, *Joule*, 2017, **1**, 155–167.

70 Y. Hu, E. M. Hutter, P. Rieder, I. Grill, J. Hanisch, M. F. Aygüler, A. G. Hufnagel, M. Handloser, T. Bein and A. Hartschuh, *Advanced Energy Materials*, 2018, **8**, 1703057.

71 M. Abdi-Jalebi, Z. Andaji-Garmaroudi, S. Cacovich, C. Stavrakas, B. Philippe, J. M. Richter, M. Alsari, E. P. Booker, E. M. Hutter and A. J. Pearson, *Nature*, 2018, **555**, 497.

72 O. G. Reid, D. T. Moore, Z. Li, D. Zhao, Y. Yan, K. Zhu and G. Rumbles, *J. Phys. D: Appl. Phys.*, 2017, **50**, 493002.

73 S. Silver, J. Yin, H. Li, J.-L. Brédas and A. Kahn, *Advanced Energy Materials*, 2018, **8**, 1703468.

74 D. B. Straus and C. R. Kagan, *The Journal of Physical Chemistry Letters*, 2018, **9**, 1434–1447.

75 O. G. Reid, M. Yang, N. Kopidakis, K. Zhu and G. Rumbles, *ACS Energy Letters*, 2016, **1**, 561–565.

Electronic Supplementary Information

Enhanced Yield-Mobility Products in Hybrid Halide Ruddlesden–Popper Compounds with Aromatic Ammonium Spacers

Naveen R. Venkatesan,[ab] Ali Mahdi,[bc] Brian Barraza,[c] Guang Wu,[c] Michael L. Chabinyc,[*ab] and Ram Seshadri[*abc]

[a] Materials Department, University of California, Santa Barbara, CA 93106, United States

[b] Materials Research Laboratory, University of California, Santa Barbara, CA 93106, United States

[c] Department of Chemistry and Biochemistry, University of California, Santa Barbara, CA 93106, United States

*Corresponding Authors: mchabinyc@engineering.ucsb.edu
seshadri@mrl.ucsb.edu

S1. Single-crystal X-ray diffraction patterns

Single-crystal X-ray diffraction data was collected using a Bruker KAPPA APEX II diffractometer equipped with an APEX II CCD detector utilizing a TRIUMPH monochromator and a Mo-Kα X-ray source (λ = 0.71703 Å). Diffraction images are shown below in Figures S1 and S2.

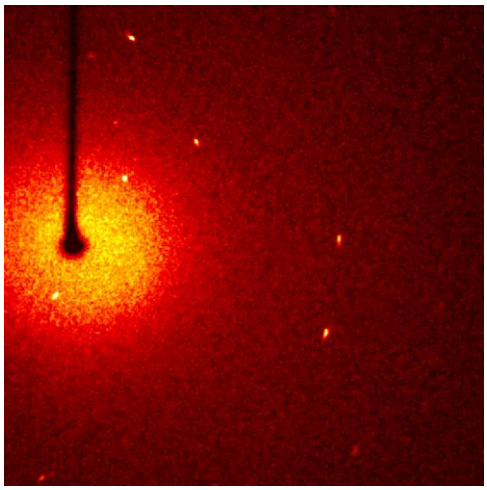

Figure S1. Sample X-ray diffraction image of $(BPEA)_2PbI_4$ obtained from grown single-crystals.

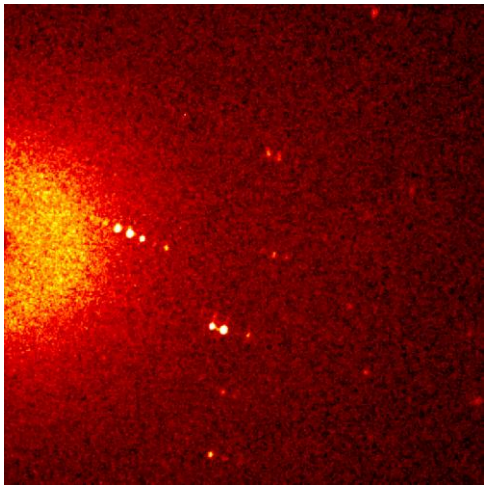

Figure S2. Sample X-ray diffraction image of $(BPEA)_2(CH_3NH_3)Pb_2I_7$ obtained from grown single-crystals.

S2. Observed bond angles and distances in $(BPEA)_2PbI_4$ and $(BPEA)_2(CH_3NH_3)Pb_2I_7$

Structural details of $(BPEA)_2PbI_4$ and $(BPEA)_2(CH_3NH_3)Pb_2I_7$ are tabulated below. Bond distances for the four equatorial and two axial iodides, along with all I-Pb-I and Pb-I-Pb (if applicable) bond angles are presented. For comparison, the bond lengths and angles from $(BA)_2PbI_4$ and $(BA)_2(MA)Pb_2I_7$ are listed in Table S2.[1]

Table S1. Structural details of $(BPEA)_2PbI_4$ and $(BPEA)_2(CH_3NH_3)Pb_2I_7$

	$(BPEA)_2PbI_4$	**$(BPEA)_2(CH_3NH_3)Pb_2I_7$**
	Bond Distances	
Pb-$I_{axial\ (1)}$ (Å)	3.2073(14)	3.131(3)
Pb-$I_{axial\ (2)}$ (Å)	3.2073(14)	3.2617(12)
Pb-$I_{axial\ (3)}$ (Å)	N/A	3.2617(12)
Pb-$I_{axial\ (4)}$ (Å)	N/A	3.131(3)
Pb-$I_{equatorial\ (1)}$ (Å)	3.108(5)	3.141(4)
Pb-$I_{equatorial\ (2)}$ (Å)	3.174(5)	3.179(3)
Pb-$I_{equatorial\ (3)}$ (Å)	3.222(5)	3.191(4)
Pb-$I_{equatorial\ (4)}$ (Å)	3.154(5)	3.157(4)
	Bond Angles	
I-Pb-$I_{axial\ (1)}$ (°)	176.4(3)	176.38(9)
I-Pb-$I_{axial\ (2)}$ (°)	N/A	176.38(9)
I-Pb-$I_{equatorial\ (1)}$ (°)	179.25(14)	176.31(8)
I-Pb-$I_{equatorial\ (2)}$ (°)	178.18(16)	176.28(9)
Pb-I-Pb_{axial} (°)	N/A	179.2(3)
Pb-I-$Pb_{equatorial}$ (°)	152.49(15)	154.52(11)

Table S2. Structural details of $(BA)_2PbI_4$ and $(BA)_2(CH_3NH_3)Pb_2I_7$ taken from reference 1.

	$(BA)_2PbI_4$	$(BA)_2(CH_3NH_3)Pb_2I_7$
	Bond Distances	
Pb-$I_{axial\ (1)}$ (Å)	3.201(16)	3.08(3)
Pb-$I_{axial\ (2)}$ (Å)	3.213(13)	3.28(3)
Pb-$I_{axial\ (3)}$ (Å)	N/A	3.25(3)
Pb-$I_{axial\ (4)}$ (Å)	N/A	3.08(3)
Pb-$I_{equatorial\ (1)}$ (Å)	3.164(7)	3.171(4)
Pb-$I_{equatorial\ (2)}$ (Å)	3.212(8)	3.169(5)
Pb-$I_{equatorial\ (3)}$ (Å)	3.191(6)	3.169(5)
Pb-$I_{equatorial\ (4)}$ (Å)	3.160(7)	3.171(4)
	Bond Angles	
I-Pb-$I_{axial\ (1)}$ (°)	178.6(3)	177.3(3)
I-Pb-$I_{axial\ (2)}$ (°)	N/A	177.3(3)
I-Pb-$I_{equatorial\ (1)}$ (°)	179.2(5)	175.5(9)
I-Pb-$I_{equatorial\ (2)}$ (°)	179.1(5)	175.5(9)
Pb-I-Pb_{axial} (°)	N/A	165.64(16)
Pb-I-$Pb_{equatorial}$ (°)	155.1(3)	164.2(10)

S3. Qualitative comparison of $(BPEA)_2(CH_3NH_3)Pb_2I_7$ with isotropic and textured XRD simulations

The single-crystal structures of $(BPEA)_2PbI_4$ and $(BPEA)_2(CH_3NH_3)Pb_2I_7$ were used to simulate powder diffraction patterns and compared with actual measurements. Figure S3 shows the comparison of $(BPEA)_2(CH_3NH_3)Pb_2I_7$ to a completely isotropic, untextured simulation of powder diffraction, showing poor agreement (isotropic $(BPEA)_2PbI_4$ is presented as the simulation in Figure 2 of the main manuscript). When texturing along the layer stacking direction ([010]) is added, the agreement between simulation and experiment is clear.

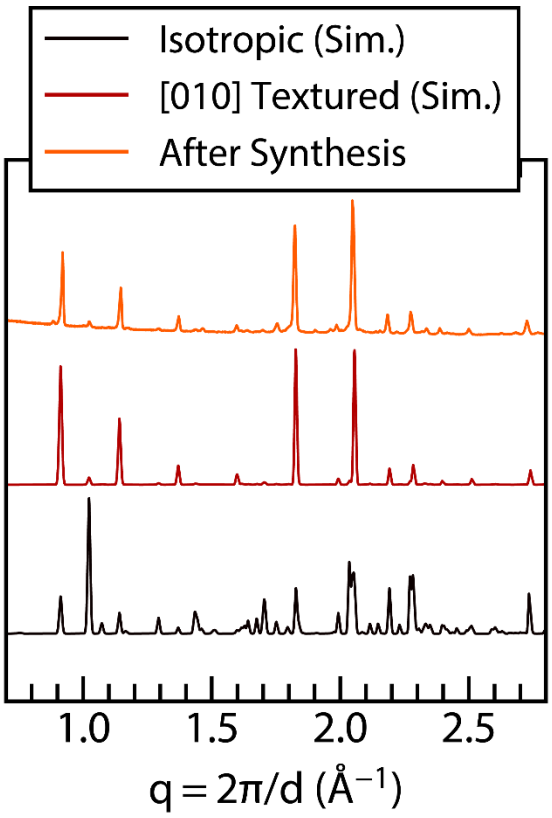

Figure S3. Powder X-ray diffraction of synthesized powder of $(BPEA)_2(CH_3NH_3)Pb_2I_7$ compared to simulated diffraction patterns of an isotropic sample and a [010]-textured sample, illustrating structural agreement with the latter.

S4. PXRD of aged powders compared to PbI_2

The aged (5 weeks in ambient) powders of $(BPEA)_2PbI_4$ and $(BPEA)_2(CH_3NH_3)Pb_2I_7$ were compared to the expected diffraction pattern of PbI_2 to show that there was no material degradation after exposure to ambient conditions.

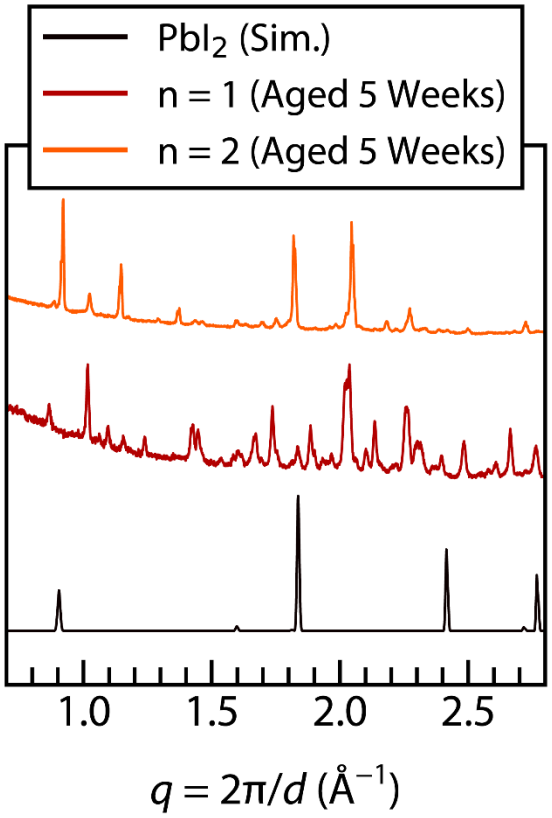

Figure S4. Powder X-ray diffraction patterns of $(BPEA)_2PbI_4$ and $(BPEA)_2(CH_3NH_3)Pb_2I_7$ powders aged for five weeks in ambient conditions, along with simulated diffraction pattern of PbI_2. Comparison with the simulated pattern illustrates no degradation of Ruddlesden–Popper phases into lead iodide.

References

1 C. C. Stoumpos, D. H. Cao, D. J. Clark, J. Young, J. M. Rondinelli, J. I. Jang, J. T. Hupp and M. G. Kanatzidis, *Chem. Mater.*, 2016, **28**, 2852–2867.